Real-Time Human Foot Motion Localization Algorithm With Dynamic Speed

Luan Van Nguyen and Hung Manh La, *Senior Member, IEEE*

***Abstract*—One challenging problem for human–machine systems is to accurately estimate the position, velocity, and attitude of human foot motion, using an inertial measurement unit (IMU) sensor. This is particularly so in large environments affected by local magnetic disturbances. In this paper, we propose an algorithm that not only handles this problem, but also works efficiently in real time. The novelty of this paper lies mainly in two contributions: First, we propose a dynamic gait phase detection (GPD) method that can detect human foot gait phase with high accuracy (2.78% errors) in dynamic speeds of human foot motion, such as walking or running; second, we integrate an inertial navigation system, a GPD, a zero velocity update, and an extended Kalman filter in real time. The system can, thus, handle the IMU drift problem, as well as noise, for high-accuracy localization both indoors (0.375% errors) and outdoors (0.55% errors). To validate the proposed algorithm, we apply the motion-tracking system (MTS-ground truth), and the results show that 93.7% of the proposed algorithm's results converge on the MTS's results within a distance of less than 7.5 cm. Hence, the proposed algorithm can be embedded in wearable sensor devices for practical applications.**

***Index Terms*—Extended Kalman filter (EKF), gait phase detection (GPD), human foot motion localization, inertial navigation system (INS), real-time localization, zero velocity update (ZVU).**

I. Introduction

INDOOR localization has many potential applications, such as searching and rescuing in emergencies, guiding visitors in navigating complex environments, security purposes, etc.

Pedestrian dead-reckoning methods [1]–[3] address the problem of tracking human foot motion by utilizing step length, velocity, and orientation. Technologies, including ultrasound, short-range radio [4]–[7], global positioning system (GPS) [8], [9], laser range scanner [10], and vision technology [11] are incorporated for higher accuracy in localization. However, their deployment is highly expensive, and their maintenance is complicated.

Human foot localization algorithms hold promise for using with inertial measurement unit (IMU) sensors [12]–[15], because the technology is not dependent on installed infrastructure; besides, they can be integrated with wearable sensor devices. For instance, IMU is used for localization and tracking of human motion [16]–[18], adopting different approaches for detection of human foot gait phase. For example, inertial navigation system (INS)+zero velocity update (ZVU) methods and Bayesian filter-based sensor fusion [1], [10], [12], [19]–[24] are used to deal with IMU drift. Additionally, unscented/extended Kalman filter (EKF) [13], [15], [25]–[28] and particle filters [29] are applied to increase the accuracy of localization. However, these approaches lead to travel distance errors of up to 10% [13], [14], particularly in environments with local magnetic disturbances. In addition, current algorithms do not run in real time and only address certain foot motion speeds; these limitations can inhibit the algorithms' practical application. For example, in our case, we are interested in developing, by applying human foot localization using an IMU sensor, a smart embedded wearable device: A smart shoe for building a real-time 3-D map [30], [31]. This requires attachment of 2-D laser range scanners and an IMU sensor to the shoe for obtaining highly accurate and real-time human foot localization. Another importance example that requires real-time dynamic foot localization is providing efficient support to monitoring of human health state and gait malady analysis [32], [33], 3-D human skeleton localization [34], human–robot interaction [35], etc.

The two main contributions of this paper are the following: 1) development of a dynamic gait phase detection (GPD) algorithm for accurate detection of human foot gait phases (swing and stance) in dynamic speeds, such as walking and running; and 2) development of a real-time and accurate foot motion localization algorithm, which can integrate the GPD with a ZVU, a heuristic heading reduction (HDR), and an EKF to address IMU drift and noise in environments affected by local magnetic disturbances.

The remainder of this paper is organized as follows. Section II presents an overview of the human foot motion localization scheme. Section III analyzes human gait motion. Section IV presents a real-time human foot motion localization algorithm. Section V applies the motion-tracking system (MTS) to verify the proposed algorithm's accuracy. Section VI presents experimental results to demonstrate the effectiveness of the proposed algorithm, besides comparing it with other existing algorithms. Finally, Section VII presents the discussion and conclusion.

II. Overview of the Human Foot Motion Localization Scheme

The overview of the human foot motion localization scheme, with three different modules, is shown in Fig. 1.

The bottom module is an IMU device with three embedded sensors: an accelerometer for measuring acceleration $\boldsymbol{a}_b^{t+1}$, a

Manuscript received April 1, 2015; revised September 6, 2015, February 5, 2016, April 29, 2016, and May 20, 2016; accepted June 6, 2016. Date of publication August 3, 2016; date of current version November 11, 2016. This work was supported in part by the University of Nevada, Reno, and in part by the National Science Foundation under Grant NSF-ICorps#1559942 and Grant NSF-NRI#1426828. This paper was recommended by Associate Editor R. van Paassen.

The authors are with the Department of Computer Science and Engineering, University of Nevada, Reno, NV 89557 USA (e-mail: luan@nevada.unr.edu; hla@unr.edu).

Color versions of one or more of the figures in this paper are available online at http://ieeexplore.ieee.org.

Digital Object Identifier 10.1109/THMS.2016.2586741

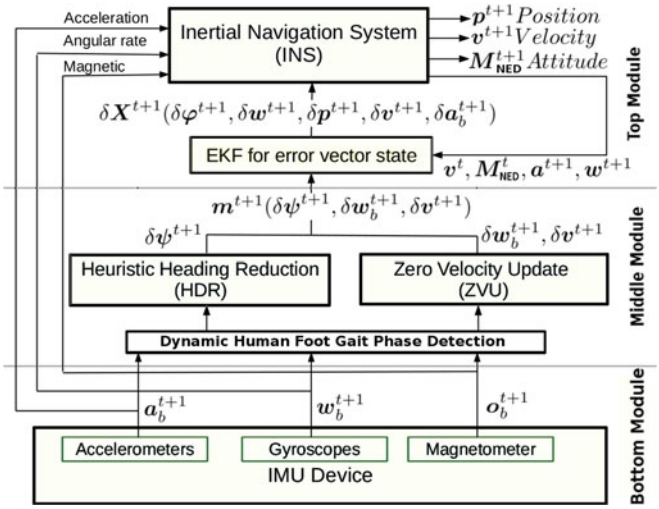

Fig. 1. INS/EKF ZVU HDR algorithm.

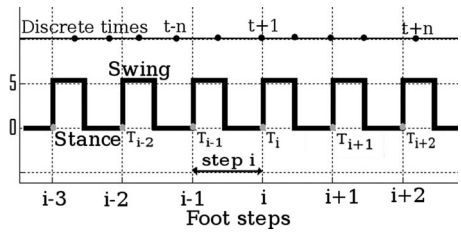

Fig. 2. Definition of subscripts and superscripts.

gyroscope for measuring angular rate $\boldsymbol{w}_b^{t+1}$, and a magnetometer for measuring magnetic field of the Earth $\boldsymbol{o}_b^{t+1}$. The subscript b in these formulas refers to the value of these variables in the body frame of the IMU device; the superscript $t+1$ refers to the value of these variables at discrete time $t+1$ in the IMU's time series, as shown in Fig. 2. Certain IMU models available in the market are integrated with the GPS, but no such integration is considered necessary to our IMU device, because we are concerned with only that localization algorithm, which works in environments that have no GPS support.

Since the IMU normally outputs the data of acceleration $\boldsymbol{a}_b^{t+1}$, angular rate $\boldsymbol{w}_b^{t+1}$, Earth's magnetic field $\boldsymbol{o}_b^{t+1}$, and the quaternion $\boldsymbol{q}^{t+1}$, we need to derive the Euler rotation angles, i.e., roll (α^{t+1}), pitch (β^{t+1}), and yaw (γ^{t+1}), from these raw data. The IMU's quaternion is a vector $\boldsymbol{q}^{t+1}(x, y, z, w)$, and the conjugation $(\boldsymbol{q}^{t+1})^*$ of $\boldsymbol{q}^{t+1}$ is a vector, which are obtained as follows:

$$(\boldsymbol{q}^{t+1})^* = (-\boldsymbol{q}^{t+1}(x), -\boldsymbol{q}^{t+1}(y), -\boldsymbol{q}^{t+1}(z), \boldsymbol{q}^{t+1}(w)). \quad (1)$$

Then, the Euler angles of rotation, i.e., α^{t+1}, β^{t+1}, and γ^{t+1}, which rotate along the X-, Y-, Z-axes, respectively, can be obtained as follows:

$$\begin{bmatrix} \alpha^{t+1} \\ \beta^{t+1} \\ \gamma^{t+1} \end{bmatrix} = \begin{bmatrix} f_1(\boldsymbol{q}^{t+1}(x)) \\ f_2(\boldsymbol{q}^{t+1}(x)) \\ f_3(\boldsymbol{q}^{t+1}(x)) \end{bmatrix} \quad (2)$$

where

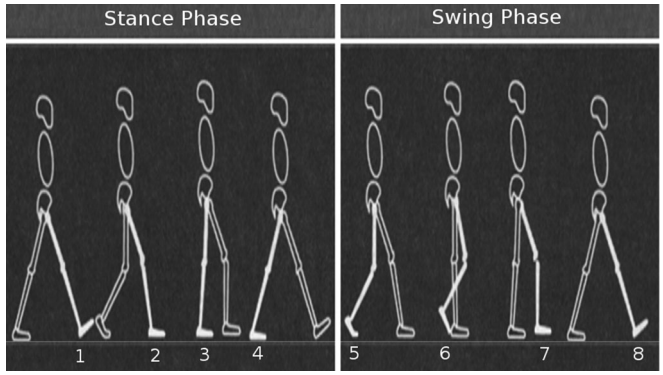

Fig. 3. Human motion gait phase.

$$\begin{aligned} f_1(\boldsymbol{q}^{t+1}) &= \text{atan2}[2(\boldsymbol{q}^{t+1}(x)\boldsymbol{q}^{t+1}(y) + \boldsymbol{q}^{t+1}(z)\boldsymbol{q}^{t+1}(w)), \\ &\quad 1 - 2((\boldsymbol{q}^{t+1}(y))^2 + (\boldsymbol{q}^{t+1}(z))^2) \\ f_2(\boldsymbol{q}^{t+1}) &= \text{arcsin}[2(\boldsymbol{q}^{t+1}(x)\boldsymbol{q}^{t+1}(z) - \boldsymbol{q}^{t+1}(w)\boldsymbol{q}^{t+1}(y)) \\ f_3(\boldsymbol{q}^{t+1}) &= \text{atan2}[2(\boldsymbol{q}^{t+1}(x)\boldsymbol{q}^{t+1}(z) + \boldsymbol{q}^{t+1}(y)\boldsymbol{q}^{t+1}(z)), \\ &\quad 1 - 2((\boldsymbol{q}^{t+1}(z))^2 + (\boldsymbol{q}^{t+1}(w))^2)]. \end{aligned}$$

The middle module includes three components: a GPD, a ZVU, and an HDR. The GPD detects the stance and swing phases of human foot gait from IMU's data. Then, the ZVU and the HDR utilize these data to estimate the error measurement vector $\boldsymbol{m}^{t+1}$, which are the most important input data for the success of the EKF algorithm. Because the EKF requires kinematically related measurements of position, velocity, and attitude, it has to rely on the supports from the GPD, the ZVU, and the HDR.

The top module includes an INS and an EKF. The INS system alone cannot cope with the IMU drift. The EKF, with a properly constructed sensor fusion, can estimate the IMU biases; therefore, it can help the conventional INS in reducing the IMU drift. The EKF estimates the errors of actual acceleration, velocity, and position of human foot motion, by taking the error measurement vector from the middle module and the feedback data from the output of the INS (see Fig. 2). On its turn, the INS receives IMU's data and the state measurement errors $\delta\boldsymbol{X}^{t+1}$ from the EKF to continuously compute, via dead reckoning, the velocity, attitude, and position of human foot motion.

III. Human Gait Motion Analysis

A. Dynamic Human Gait Phase Detection

Obtaining high accuracy in human motion localization, using IMU sensors, is challenging because it depends greatly on multiple factors: the drift of the IMU sensors, its position on the Earth, and the local magnetic disturbances from the external environment. Fortunately, human foot motion gait comprises two phases, i.e., stance and swing [36], [37], as shown in Fig. 3, which can be utilized to estimate IMU drift and the effects of environment. In the stance phase, the human foot stands on the ground, and therefore, its actual velocity is zero. Hence, if the IMU's velocity of foot in this phase is different from zero, it

must be the error due to IMU's drift. Therefore, we can apply the ZVU algorithm to reduce IMU's drift and enhance the accuracy of localization. Therefore, the accuracy of the stance phase detection, in real time, is crucial to obtaining higher accuracy of human foot localization. Furthermore, the accuracy of human foot motion GPD depends on a person's physical characteristics and foot motion speeds. This leads to a very important question as to how to detect the stance phase accurately in dynamic motion speeds.

However, the current algorithms do not run in real time and only address certain human foot motion speeds. For example, the algorithm in [14] is limited to normal walking speed and that in [13] to offline GPD, which relies on predefined thresholds of acceleration and angular rate. Hence, these algorithms may not work for different human characteristics and speeds of foot motion, in real time.

To solve this problem, we propose an efficient method that automatically computes and updates threshold values through real-time operation and varying foot motion speeds. Therefore, the proposed algorithm can effectively detect human foot motion gait phase in different speeds, such as walking and running.

First, we present the dynamics of sensor data $d_{g.i}^{t+1}$ at time $t+1$ of ith foot step from the changes in local acceleration ($|\boldsymbol{a}_{\text{local.i}}^{t+1} - \boldsymbol{a}_{\text{local.i}}^{t}|$), magnitude of acceleration ($|\boldsymbol{a}_{m.i}^{t+1} - \boldsymbol{a}_{m.i}^{t}|$), and angular rate magnitude ($|\boldsymbol{w}_{m.i}^{t+1} - \boldsymbol{w}_{m.i}^{t}|$) as follows:

$$d_{g.i}^{t+1} = |\boldsymbol{a}_{m.i}^{t+1} - \boldsymbol{a}_{m.i}^{t}| + |\boldsymbol{a}_{\text{local.i}}^{t+1} - \boldsymbol{a}_{\text{local.i}}^{t}| + |\boldsymbol{w}_{m.i}^{t+1} - \boldsymbol{w}_{m.i}^{t}| \tag{3}$$

where the real motion of acceleration in the North East Down (NED) of the Earth coordinate system [14], [38] can be obtained as follows:

$$\boldsymbol{a}_{m.i}^{t+1} = \boldsymbol{a}_{e.i}^{t+1} - \boldsymbol{g}_e \tag{4}$$

where $\boldsymbol{g}_e$ is the gravitational acceleration vector

$$\boldsymbol{g}_e = (0.0, 0.0, 9.8\ \text{m/s}^2) \tag{5}$$

and the acceleration of motion in the NED system can be obtained as follows:

$$\boldsymbol{a}_{e.i}^{t+1} = \boldsymbol{q}^{t+1}.\boldsymbol{a}_{b.i}^{t+1}.(\boldsymbol{q}^{t+1})^* \tag{6}$$

where $\boldsymbol{a}_{b.i}^{t+1}$ is the acceleration of the IMU in its body frame at time $t+1$ of the ith foot step.

The local acceleration $\boldsymbol{a}_{\text{local.i}}^{t+1}$ is obtained as follows:

$$(\boldsymbol{a}_{\text{local.i}}^{t+1})^2 = \frac{1}{2f+1} \sum_{j=t-2f}^{t+1} (\boldsymbol{a}_{b.i}^{t+1} - \boldsymbol{a}_{\text{ave.i}}^{j})^2. \tag{7}$$

It is to be noted that (7) is computed in real time. The main difference, compared with the current offline algorithms [13]–[15], is that this formula requires only data for computing local acceleration from some immediately preceding steps. The superscript j in (7) represents data from time step $t+1$, dating back to the previous time steps $2f+1$ (for example, $f = 15$ steps).

The average acceleration $\boldsymbol{a}_{\text{ave.i}}^{j}$ in (7) is, thus, computed as

$$\boldsymbol{a}_{\text{ave.i}}^{j} = \frac{1}{2f+1} \sum_{k=j-2f-1}^{j} \boldsymbol{a}_{b.i}^{k}. \tag{8}$$

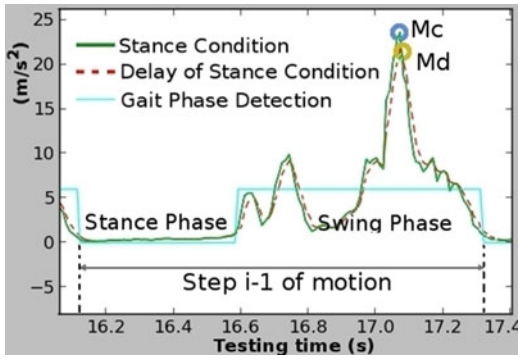

Fig. 4. Human gait phases detection at foot step $i-1$.

Then, the dynamic gain $d_{g.i}^{t+1}$ (at time $t+1$ of ith foot step) is used to compute the values of stance condition $s_{c.i}^{t+1}$ from some previous and current values of $d_{g.i}^{t+1}$:

$$s_{c.i}^{t+1} = \frac{d_{g.i}^{t+1} + d_{g.i}^{t} + d_{g.i}^{t-1} + d_{g.i}^{t-2} + d_{g.i}^{t-3}}{5}. \tag{9}$$

It is to be noted that (9) uses five previous and current values of $d_{g.i}^{t+1}$, but this can be changed depending on the type of IMU.

If $t+1$ is a discretized time during the ith foot step of the foot motion, then the delay of the stance condition $s_{d.i}^{t+1}$ of $s_{c.i}^{t+1}$ is obtained as follows:

$$s_{d.i}^{t+1} = \frac{s_{d.i}^{t-1} + s_{c.i}^{t+1}}{2} \tag{10}$$

where the initial value of $s_{d.i}^{0}$ can be initiated by 0.8, which is the experimental result of a threshold of normal walking speed.

If $\max_{cd.i}^{t+1}$ is the max changing speed for the difference between $s_{d.i}^{t+1}$ and $s_{c.i}^{t+1}$, then we have

$$\max_{cd.i}^{t+1} = \begin{cases} s_{c.i}^{t+1}, & s_{d.i}^{t+1} \le s_{c.i}^{t+1} \\ s_{d.i}^{t+1}, & \text{otherwise.} \end{cases} \tag{11}$$

Let us define $\boldsymbol{s}_{c.(i-1)}$ as an array of all discretized points $s_{c.(i-1)}^{t+1}$ (the green line in the swing phase of Fig. 4), and $\boldsymbol{s}_{d.(i-1)}$ as an array of all discretized points $s_{d.(i-1)}^{t+1}$ during the swing phase of the foot step $i-1$ (the red-dashed line in the swing phase of Fig. 4).

The maximum value of the stance condition $s_{c.(i-1)}^{t+1}$, during the swing phase of the $i-1$ foot step, $Mc(\boldsymbol{s}_{c.(i-1)})$, is, thus, computed as

$$Mc(\boldsymbol{s}_{c.(i-1)}) = \text{Max}\{s_{c.(i-1)}^{t+1} | s_{c.(i-1)}^{t+1} \in \boldsymbol{s}_{c.(i-1)}\}. \tag{12}$$

In Fig. 4, Mc point is inside the blue circle with the Mc label.

Similarly, the maximum value of the delay of the stance condition $s_{d.(i-1)}^{t+1}$, during the swing phase of the $i-1$ foot step, i.e., $Md(\boldsymbol{s}_{d.(i-1)})$, is, thus, obtained as

$$Md(\boldsymbol{s}_{d.(i-1)}) = \text{Max}\{s_{d.(i-1)}^{t+1} | s_{d.(i-1)}^{t+1} \in \boldsymbol{s}_{d.(i-1)}\}. \tag{13}$$

In Fig. 4, Md point is inside the yellow circle with the Md label.

The dynamic threshold th^i of the ith foot step is obtained as follows:

$$\text{th}^i = Mc(\boldsymbol{s}_{c.(i-1)}) - Md(\boldsymbol{s}_{d.(i-1)}) \tag{14}$$

where the initial value of th^0 depends on the IMU sensor, which, in this case, is 0.8, the experimental threshold of a normal walking speed. In general, for an arbitrary IMU, the initial threshold value can be selected from 0.5 to 1. Since th^i is a dynamic threshold, it helps the human foot motion localization algorithm in adapting to speed changes in foot motion. This threshold is free from any predefined threshold value and depends only on the speed of motion. It increases when the motion speed increases and vice versa. Hence, it can work with any person's gait and different motion speeds like walking or running.

From (14), we can obtain the dynamic human gait detection g_d^{t+1} as follows:

$$g_{d.i}^{t+1} = \begin{cases} 0, & \max_{cd.i}^{t+1} \leq \text{th}^i \text{ (stance phase)} \\ 6, & \text{otherwise (swing phase)} \end{cases} \tag{15}$$

when $g_{d.i}^{t+1} = 0$, the gait is in the stance phase, and when $g_{d.i}^{t+1} = 6$, it is in the swing phase.

The summary of the dynamic gate phase (DGP) detection algorithm is presented in Algorithm 1.

We tested the DGP detection algorithm with different walking and running speeds in the hallway on the first floor of the Applied Research Facility building, University of Nevada, Reno (UNR) campus. The results of this test in detecting the swing and stance phases are shown in Fig. 5.

The experimental results [see Fig. 5(b)] are collected for different human foot speeds: slow walk (0.85 m/s), normal walk (1.38 m/s), fast walk (1.92 m/s), and slow run (5.7 m/s). The peaks of max changing speed [blue line in Fig. 5(a)] clearly change, following the speed change. The dynamic threshold values [green line in Fig. 5(a)] are updated and adapted after each gait circle of this test. As a result, the DGP algorithm can detect the human foot gait phases [red line in Fig. 5(a)] correctly. The average error, detected from over 50 different DGP tests, is 1 in 36 steps, which is equivalent to 2.78%.

B. Zero Velocity Update Algorithm

As mentioned in Section III-B, whenever the GPD algorithm detects the stance phase of human foot motion gait, the ZVU algorithm [12], [13], [15] can measure the bias velocity, which helps in fixing the error due to IMU's drift. Hence, the ZVU algorithm is important in enhancing the accuracy of the human foot localization by using IMUs. Without loss of generality, we can assume that each gait of human foot motion occurs over a duration of $[T_i - \delta T_i, T_i]$, where T_i is the discrete time at the end of the stance phase of the ith foot step, as shown in Fig. 2. The bias error a_{be}^{t+1} of acceleration at time $t+1 = T_i$ of foot motion in the stance phase can be obtained as follows:

$$\boldsymbol{a}_{\text{mbe}}^{t+1} = \frac{\boldsymbol{v}_m^{t+1=T_i}}{\delta T_i}. \tag{16}$$

Then, from (16), the bias error of acceleration in the NED system can, thus, be obtained as

$$\boldsymbol{a}_{\text{ebe}}^{t+1} = \boldsymbol{a}_{\text{mbe}}^{t+1} + \boldsymbol{g}_e. \tag{17}$$

Algorithm 1: DYNAMIC HUMAN GAIT PHASE (DGP) DETECTION.

Input: Real-time acceleration, angular rate vectors at discrete times $t+1$ of the foot step i_{th} in IMU body system $\langle a_{b.i}^{t+1}, w_{b.i}^{t+1} \rangle$

Output: $True$:Stance Phase, $False$:Swing Phase

if $t+1 \geq 2f+1$ **then**
  //The local acceleration; $j \leftarrow t$
  while $(j \leq t) and (j \geq (t-f))$ **do**
    $k \leftarrow (j-f)$
    while $k \leq j$ **do**
      $\boldsymbol{a}_{ave.i}^j \leftarrow \boldsymbol{a}_{ave.i}^j + \boldsymbol{a}_{b.i}^k$
      $k \leftarrow (k+1)$
    $\boldsymbol{a}_{ave.i}^j \leftarrow \frac{1}{2f+1} \boldsymbol{a}_{ave.i}^j$
    $(\boldsymbol{a}_{local.i}^{t+1})^2 \leftarrow (\boldsymbol{a}_{local.i}^{t+1})^2 + (\boldsymbol{a}_{b.i}^{t+1} - \boldsymbol{a}_{ave.i}^j)^2$
    $j \leftarrow (j-1)$
  $(\boldsymbol{a}_{local.i}^{t+1})^2 \leftarrow \frac{1}{2f+1} (\boldsymbol{a}_{local.i}^{t+1})^2$
else
  $j \leftarrow t$
  $k \leftarrow 0$
  while $k \leq j$ **do**
    $\boldsymbol{a}_{ave.i}^j \leftarrow \boldsymbol{a}_{ave.i}^j + \boldsymbol{a}_{b.i}^k$
    $k \leftarrow (k+1)$
  $(\boldsymbol{a}_{local.i}^{t+1})^2 \leftarrow \frac{1}{k+1} \boldsymbol{a}_{ave.i}^j$
//The dynamics of sensor data; $d_{g.i}^{t+1} \leftarrow |\boldsymbol{a}_{local.i}^{t+1} - \boldsymbol{a}_{local.i}^t| + |\boldsymbol{a}_{m.i}^{t+1} - \boldsymbol{a}_{m.i}^t| + |\boldsymbol{w}_{m.i}^{t+1} - \boldsymbol{w}_{m.i}^t|$
//The stance condition; $s_{c.i}^{t+1} \leftarrow \frac{d_{g.i}^{t+1} + d_{g.i}^t + d_{g.i}^{t-1} + d_{g.i}^{t-2} + d_{g.i}^{t-3}}{5}$
//The delay of the stance condition; $s_{d.i}^{t+1} \leftarrow \frac{s_{d.i}^{t-1} + s_{c.i}^{t+1}}{2}$
//The max changing speed
if $s_{d.i}^{t+1} \leq s_{c.i}^{t+1}$ **then**
  $max_{cd.i}^{t+1} \leftarrow s_{c.i}^{t+1}$;
else
  $max_{cd.i}^{t+1} \leftarrow s_{d.i}^{t+1}$;
//The a maximum value of the stance condition; $Mc(\boldsymbol{s}_{c.(i-1)}) \leftarrow Max\{s_{c.(i-1)}^{t+1} | s_{c.(i-1)}^{t+1} \in \boldsymbol{s}_{c.(i-1)}\}$
$Md(\boldsymbol{s}_{d.(i-1)}) \leftarrow Max\{s_{d.(i-1)}^{t+1} | s_{d.(i-1)}^{t+1} \in \boldsymbol{s}_{d.(i-1)}\}$
//The dynamic threshold; $th^i \leftarrow (Mc(\boldsymbol{s}_{c.(i-1)}) - Md(\boldsymbol{s}_{d.(i-1)}))$
//The dynamic human gait detection
if $max_{cd.i}^{t+1} \leq th^i$ **then**
  return *True*
else
  return *False*

We can now compute the bias error of acceleration in the IMU body frame as

$$\boldsymbol{a}_{\text{bbe}}^{t+1} = (\boldsymbol{q}^{t+1})^* . \boldsymbol{a}_{\text{ebe}}^{t+1} . \boldsymbol{q}^{t+1}. \tag{18}$$

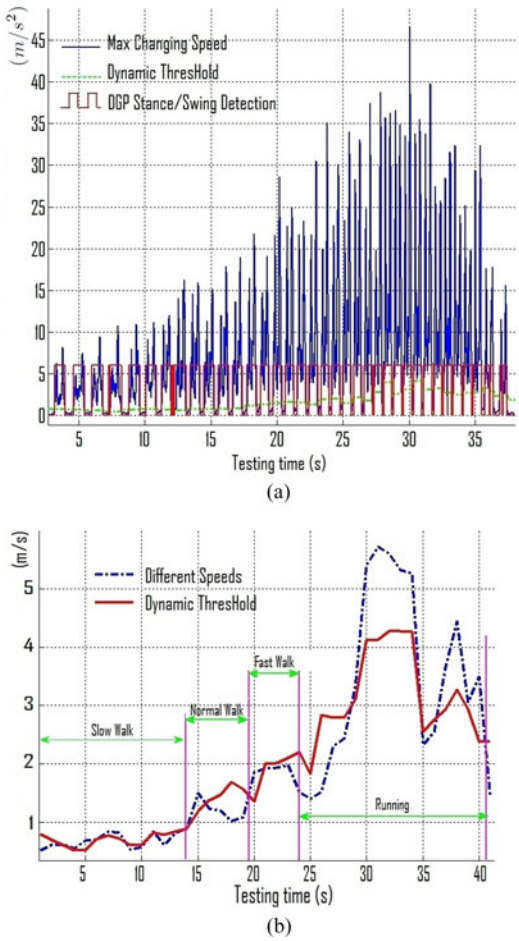

Fig. 5. Dynamic human GPD with different speeds.

From (18), we can extract the bias error velocity, which is also the drifted velocity $\delta \boldsymbol{v}^{t+1}$, in the body frame as follows:

$$\delta \boldsymbol{v}_b^{t+1} = \boldsymbol{v}_{\text{bbe}}^{t+1} = \int \boldsymbol{a}_{\text{bbe}}^{t+1} dt. \tag{19}$$

The actual motion value of acceleration $\boldsymbol{a}_a^{t+1}$ can, thus, be calculated as

$$\boldsymbol{a}_a^{t+1} = \boldsymbol{a}_m^{t+1} - \boldsymbol{a}_{\text{mbe}}^{t+1}. \tag{20}$$

The actual velocity and position of the human foot motion can be obtained as follows:

$$\boldsymbol{v}_a^{t+1} = \int \boldsymbol{a}_a^{t+1} dt \tag{21}$$

$$\boldsymbol{p}_a^{t+1} = \int \boldsymbol{v}_a^{t+1} dt. \tag{22}$$

C. Heuristic Heading Reduction

It is to be noted that human foot motion usually occurs in a straight direction. For this reason, an HDR algorithm [13], [39] is applied to adjust the drifted yaw(γ) angle of heading direction. If the magnetic field of environment changes the heading direction, that would affect the bias of γ angle. Hence, we can rely on comparing the γ angle at time step T_i with the two previous γ angles, at time steps $T_{(i-1)}$ and $T_{(i-2)}$. The result helps adjust the bias of γ angle as follows:

$$\delta\psi^{t+1} = \delta\psi_{\gamma^{T_i}} = \gamma^{T_i} - \frac{\gamma^{T_{(i-1)}} + \gamma^{T_{(i-2)}}}{2} \tag{23}$$

where T_i is the last discrete time of the stance phase of the ith foot step (see Fig. 2).

The HDR adjusts the straight bias of γ angle at each discrete time $t+1$ for accelerating the swing phase as follows:

$$\delta\psi^{t+1} = \begin{cases} \delta\psi^{t+1}, & \delta\psi^{t+1} \leq \text{th}_\gamma \\ 0, & \text{otherwise} \end{cases} \tag{24}$$

where the threshold value ($\text{th}_\gamma = 0.5$ rad) is chosen depending on the outcome of the experiment.

After applying the HDR algorithm, the acceleration at the swing phase of each time step needs to be updated as follows:

$$\boldsymbol{a}_{e\text{HDR}}^{t+1} = \boldsymbol{M}_{\text{NED}}^{1|0} . \boldsymbol{a}_b^{t+1} \tag{25}$$

where $\boldsymbol{M}_{\text{NED}}^{1|0}$ can be obtained from (39), but α, β, and γ in this equation need to be updated as follows:

$$\alpha = \alpha^{t+1}, \quad \beta = \beta^{t+1}, \quad \gamma = \gamma^{t+1} + \delta\psi^{t+1} \tag{26}$$

where α^{t+1}, β^{t+1}, and γ^{t+1} are as given by (2).

The real motion acceleration in the NED system can be obtained as follows:

$$\boldsymbol{a}_{m\,\text{HDR}}^{t+1} = \boldsymbol{a}_{e\text{HDR}}^{t+1} - \boldsymbol{g}_e \tag{27}$$

where $\boldsymbol{g}_e$ is as given by (5).

In addition, when we apply the HDR and INS/ZVU algorithm for actual velocity and position, (21)–(22) will have to be computed again by using the new actual acceleration $\boldsymbol{a}_{m\,\text{HDR}}^{t+1}$.

IV. Real-Time Human Foot Motion Localization Algorithm With Dynamic Speed

In this section, we present the real-time human foot motion localization algorithm by applying the proposed method for dynamic gait detection. We name it as real-time dynamic INS/EKF+ZVU+HDR algorithm and show its diagram in Fig. 6.

In this diagram, whenever the DGP algorithm detects a stance phase of gait at time $t+1$, the ZVU and the HDR algorithms estimate the vector $\boldsymbol{m}^{t+1}$ of the actual error measurement for EKF's input data as

$$\boldsymbol{m}^{t+1} = (\delta\psi^{t+1}, \delta\boldsymbol{w}_b^{t+1}, \delta\boldsymbol{v}_b^{t+1}) \tag{28}$$

where the bias of yaw angle $\delta\psi^{t+1}$ is obtained by the HDR algorithm as in (23), and the bias error of velocity is obtained as follows:

$$\delta\boldsymbol{v}_b^{t+1} = \boldsymbol{v}_b^{t+1} - \boldsymbol{v}_a^{t+1} \tag{29}$$

where $\boldsymbol{v}_b^{t+1}$ is obtained by the ZVU algorithm in (19), $\boldsymbol{v}_a^{t+1}$ is the actual velocity of the foot in the stance phase, or $\boldsymbol{v}_a^{t+1} = [0\,0\,0]^T$,

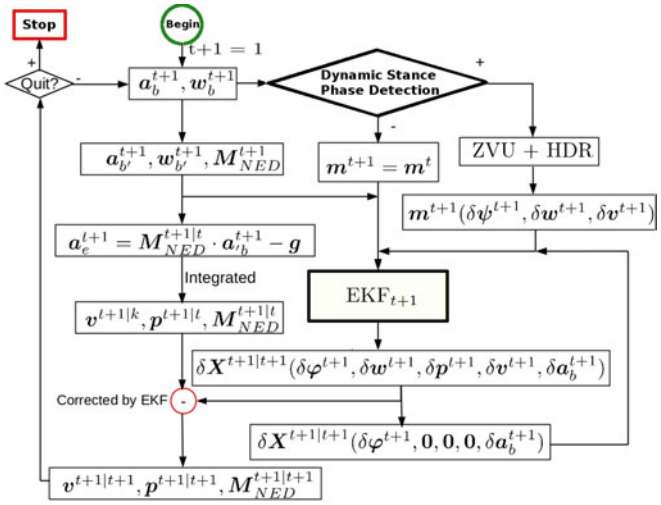

Fig. 6. Real-time dynamic INS/EKF+ZVU+HDR algorithm.

and the bias error angular rate is obtained as follows:

$$\delta \boldsymbol{w}_b^{t+1} = \boldsymbol{w}_b^{t+1} - \boldsymbol{w}_a^{t+1} \tag{30}$$

where $\boldsymbol{w}_a^{t+1}$ is the actual angular rate of the foot in the stance phase, or $\boldsymbol{w}_a^{t+1} = [0\ 0\ 0]^T$.

The EKF's error state vector [13], [15] at the previous time t is a 15-element vector $\delta \boldsymbol{X}^{t|t}$, and its function corrects the INS's output values: the velocity, the position, and the attitude, as shown in Fig. 1

$$\delta \boldsymbol{X}^{t|t} = \delta \boldsymbol{X}^t(\delta \boldsymbol{\varphi}^t, \delta \boldsymbol{w}^t, \delta \boldsymbol{p}^t, \delta \boldsymbol{v}^t, \delta \boldsymbol{a}_b^t) \tag{31}$$

where $\delta \boldsymbol{\varphi}^t$, $\delta \boldsymbol{w}^t$, $\delta \boldsymbol{p}^t$, $\delta \boldsymbol{v}^t$, and $\delta \boldsymbol{a}_b^t$ represent the EKF's estimated errors of attitude, angular rate, position, velocity, and acceleration at time t, respectively.

The EKF's predicted error state vector at time $t+1$ is given by

$$\delta \boldsymbol{X}^{t+1|t} = \boldsymbol{\Phi}^{t+1} \delta \boldsymbol{X}^{t|t} + \boldsymbol{n}_p^t \tag{32}$$

where $\delta \boldsymbol{X}^{t|t}$ is the EKF's error state vector at previous time t, and $\boldsymbol{n}_p^t$ is the process noise assumed to be zero mean Gaussian white noise with covariance matrix $\boldsymbol{Q}^t$: $\boldsymbol{n}_p^t \hookrightarrow (0, \boldsymbol{Q}^t)$, $\boldsymbol{Q}^t = \boldsymbol{E}(\boldsymbol{n}_p^t (\boldsymbol{n}_p^t)^T)$. The selection of $\boldsymbol{Q}^t$ is given in Section VI.

The EKF's state transition matrix, $\boldsymbol{\Phi}^{t+1}$, is a 15×15 matrix

$$\boldsymbol{\Phi}^{t+1} = \begin{bmatrix} \boldsymbol{I} & \Delta t \cdot \boldsymbol{M}_{NED}^{t+1|t} & \boldsymbol{0} & \boldsymbol{0} & \boldsymbol{0} \\ \boldsymbol{0} & \boldsymbol{I} & \boldsymbol{0} & \boldsymbol{0} & \boldsymbol{0} \\ \boldsymbol{0} & \boldsymbol{0} & \boldsymbol{I} & \Delta t \cdot \boldsymbol{I} & \frac{-\Delta t^2}{2} \cdot \boldsymbol{S}(a_{n'}^{t+1}) \\ -\Delta t \cdot \boldsymbol{S}(a_{n'}^{t+1}) & \boldsymbol{0} & \boldsymbol{0} & \boldsymbol{I} & \Delta t \cdot \boldsymbol{M}_{NED}^{t+1|t} \\ \boldsymbol{0} & \boldsymbol{0} & \boldsymbol{0} & \boldsymbol{0} & -\Delta t \cdot \boldsymbol{S}(a_{n'}^{t+1}) \end{bmatrix} \tag{33}$$

where $\boldsymbol{I}$ is a 3×3 unit matrix, and $\boldsymbol{0}$ is a 3×3 zero matrix. $\boldsymbol{S}(a_{n'}^{t+1})$ is a skew-symmetric matrix of the following accelerations:

$$\boldsymbol{S}(\boldsymbol{a}_{n'}^{t+1}) = \begin{bmatrix} 0 & -\boldsymbol{a}_{n'}^{t+1}(2) & \boldsymbol{a}_{n'}^{t+1}(1) \\ \boldsymbol{a}_{n'}^{t+1}(2) & 0 & -\boldsymbol{a}_{n'}^{t+1}(2) \\ -\boldsymbol{a}_{n'}^{t+1}(1) & \boldsymbol{a}_{n'}^{t+1}(0) & 0 \end{bmatrix} \tag{34}$$

where $\boldsymbol{a}_{n'}^{t+1}$ is the bias-corrected acceleration in the NED frame:

$$\boldsymbol{a}_{n'}^{t+1} = \boldsymbol{M}_{\text{NED}}^{t+1|t} \cdot \boldsymbol{a}_{b'}^{t+1}. \tag{35}$$

Here $\boldsymbol{M}_{\text{NED}}^{t+1|t}$ is a transformation matrix, as given in (37).

The bias compensations for acceleration $\boldsymbol{a}_{b'}^{t+1}$ and angular rate $\boldsymbol{w}_{b'}^{t+1}$ are obtained from the EKF error state vector $\delta \boldsymbol{X}^{t|t}$ in (31), as follows:

$$\boldsymbol{w}_{b'}^{t+1} = \boldsymbol{w}_b^{t+1} - \delta \boldsymbol{w}_b^{t+1} \tag{36a}$$

$$\boldsymbol{a}_{b'}^{t+1} = \boldsymbol{a}_b^{t+1} - \delta \boldsymbol{a}_b^{t+1} \tag{36b}$$

where the raw data of acceleration $\boldsymbol{a}_b^{t+1}$ and the angular rate $\boldsymbol{w}_b^{t+1}$ here are in the IMU's body frame.

The transformation matrix [13], [15] $\boldsymbol{M}_{\text{NED}}^{t+1|t}$ that transforms the data from IMU's body frame into NED's frame is obtained as follows:

$$\boldsymbol{M}_{\text{NED}}^{t+1|t} = \boldsymbol{M}_{\text{NED}}^{t|t} \cdot \frac{2\boldsymbol{I}_{3\times 3} + \delta \boldsymbol{\Omega}_t \cdot \Delta t}{2\boldsymbol{I}_{3\times 3} - \delta \boldsymbol{\Omega}_t \cdot \Delta t} \tag{37}$$

where $\delta \boldsymbol{\Omega}_t$ is a skew-symmetric matrix of the following angular rate:

$$\delta \boldsymbol{\Omega}_t = \begin{bmatrix} \boldsymbol{0} & -\boldsymbol{w}_{b'}^t(2) & \boldsymbol{w}_{b'}^t(1) \\ \boldsymbol{w}_{b'}^t(2) & \boldsymbol{0} & -\boldsymbol{w}_{b'}^t(0) \\ -\boldsymbol{w}_{b'}^t(1) & \boldsymbol{w}_{b'}^t(0) & \boldsymbol{0} \end{bmatrix} \tag{38}$$

where $\boldsymbol{w}_{b'}^t$ is computed by (36a), and $\boldsymbol{M}_{\text{NED}}^{t|t}$ is the last rotation matrix, updated by EKF at the previous step t. At the first time, $t+1 = 1$, the $\boldsymbol{M}_{\text{NED}}^{1|0}$ is estimated as (39), shown at the bottom of the page. Here , c, s, α, β and γ are cosine(), sine(), roll (α^1), pitch (β^1), and yaw (γ^1), respectively.

$$\boldsymbol{M}_{NED}^{1|0} = \begin{bmatrix} c(\gamma)c(\beta) & c(\gamma)s(\alpha)s(\beta) - c(\alpha)s(\gamma) & s(\alpha)s(\gamma) + c(\alpha)c(\gamma)s(\beta) \\ c(\beta)s(\gamma) & c(\alpha)c(\gamma) + s(\alpha)s(\gamma)s(\beta) & c(\alpha)s(\gamma)s(\beta) - c(\gamma)s(\alpha) \\ -s(\beta) & c(\beta)s(\alpha) & c(\alpha)c(\beta) \end{bmatrix} \tag{39}$$

The EKF's error state at time $t+1$ can be obtained by

$$\delta \boldsymbol{X}^{t+1|t+1} = \delta \boldsymbol{X}^{t+1|t} + \boldsymbol{K}^{t+1} \cdot [\boldsymbol{m}^{t+1} - \boldsymbol{H}\delta \boldsymbol{X}^{t+1|t}] \quad (40)$$

where $\boldsymbol{K}^{t+1}$ is the Kalman gain defined in (43) and $\boldsymbol{m}^{t+1}$ in (28); $\boldsymbol{H}$ is a measurement matrix

$$\boldsymbol{H}_{7\times 15} = \begin{bmatrix} \boldsymbol{O}^1_{1\times 3} & \boldsymbol{O}^0_{1\times 3} & \boldsymbol{O}^0_{1\times 3} & \boldsymbol{O}^0_{1\times 3} & \boldsymbol{O}^0_{1\times 3} \\ \boldsymbol{O}_{3\times 3} & \boldsymbol{I}_{3\times 3} & \boldsymbol{O}_{3\times 3} & \boldsymbol{O}_{3\times 3} & \boldsymbol{O}_{3\times 3} \\ \boldsymbol{O}_{3\times 3} & \boldsymbol{O}_{3\times 3} & \boldsymbol{O}_{3\times 3} & \boldsymbol{I}_{3\times 3} & \boldsymbol{O}_{3\times 3} \end{bmatrix} \quad (41)$$

where $\boldsymbol{O}^1_{1\times 3} = [0\ 0\ 1]$, $\boldsymbol{O}^0_{1\times 3} = [0\ 0\ 0]$, $\boldsymbol{I}_{3\times 3}$ is a 3×3 unit matrix, and $\boldsymbol{O}_{3\times 3}$ is a 3×3 zero matrix.

The EKF's measurement model is defined by

$$\boldsymbol{z}^{t+1} = \boldsymbol{H}\delta \boldsymbol{X}^{t+1|t+1} + \boldsymbol{n}_z^{t+1} \quad (42)$$

where $\boldsymbol{n}_z^{t+1}$ is the measurement noise with the covariance matrix $\boldsymbol{R}^{t+1} = \boldsymbol{E}(\boldsymbol{n}_z^{t+1}(\boldsymbol{n}_z^{t+1})^T)$. The value of $\boldsymbol{R}^{t+1}$ can be obtained from the real-time output data of the IMU's covariances provided by the vendor. $\boldsymbol{R}^{t+1} = \text{diag}(C^{t+1}_{o_1}, C^{t+1}_{o_2}, C^{t+1}_{o_3}, C^{t+1}_{o_1}, C^{t+1}_{o_2}, C^{t+1}_{o_3}, C^{t+1}_{o_1})$, where $C^t_{o_i}$ $(i = 1, 2, 3)$ is the value of diag matrix of orientation covariance of IMU.

The Kalman gain is obtained as follows:

$$\boldsymbol{K}^{t+1} = \boldsymbol{P}^{t+1|t}\boldsymbol{H}^T(\boldsymbol{H}\boldsymbol{P}^{t+1|t}\boldsymbol{H}^T + \boldsymbol{R}^{t+1})^{-1} \quad (43)$$

where $\boldsymbol{P}^{t+1|t}$ is an estimated error covariance matrix, computed at time $t+1$ of the IMU's output sequence. The value of $\boldsymbol{P}^{0|0}$ can be obtained from real-time output data of the IMU's covariances, provided by the vendor. $\boldsymbol{P}^{0|0} = \text{diag}(0, 0, 0, C^0_{a_1}, C^0_{a_2}, C^0_{a_3}, 0, 0, 0, 0, 0, 0, C^0_{a_1}, C^0_{a_2}, C^0_{a_3})$, where $C^0_{a_i}$ $(i = 1, 2, 3)$ is the value of diag matrix of linear acceleration covariance of IMU

$$\boldsymbol{P}^{t+1|t} = \Phi^t \boldsymbol{P}^{t|t}(\Phi^t)^T + \boldsymbol{Q}^t \quad (44)$$

where Q^t is a process noise covariance matrix; the previous $\boldsymbol{P}^{t|t}$ is computed by

$$\boldsymbol{P}^{t|t} = \left(\boldsymbol{I}_{15\times 15} - \boldsymbol{K}^t\boldsymbol{H}\right)\boldsymbol{P}^{t|t-1}\left(\boldsymbol{I}_{15\times 15} - \boldsymbol{K}^t\boldsymbol{H}\right)^T + \boldsymbol{K}^t\boldsymbol{R}^t\left(\boldsymbol{K}^t\right)^T. \quad (45)$$

Now, the acceleration $\boldsymbol{a}_e^{t+1}$ of human motion in the NED frame can be obtained by transforming the bias-compensated acceleration from (36b) to the NED frame and then subtracting the vector $\boldsymbol{g}_e$ from it as follows:

$$\boldsymbol{a}_e^{t+1} = \boldsymbol{M}_{\text{NED}}^{t+1|t} \cdot \boldsymbol{a}_{b'}^{t+1} - \boldsymbol{g}_e. \quad (46)$$

The predicted velocity of EKF in the NED frame at time $t+1$ is integrated from the motion acceleration as follows:

$$\boldsymbol{v}^{t+1|t} = \boldsymbol{v}^{t|t} + \boldsymbol{a}_e^{t+1} \cdot \Delta t. \quad (47)$$

This velocity is integrated one more time to compute the foot position in the NED frame as

$$\boldsymbol{p}^{t+1|t} = \boldsymbol{p}^{t|t} + \boldsymbol{v}^{t+1|t} \cdot \Delta t. \quad (48)$$

Finally, we can use the EKF's error state vector in (40) to adjust the values of the velocity in (47), the position in (48), and the attitude in (37)

$$\boldsymbol{v}^{t+1|t+1} = \boldsymbol{v}^{t+1|t} - \delta \boldsymbol{v}^{t+1|t+1} \quad (49)$$

$$\boldsymbol{p}^{t+1|t+1} = \boldsymbol{p}^{t+1|t} - \delta \boldsymbol{p}^{t+1|t+1} \quad (50)$$

$$\boldsymbol{M}_{\text{NED}}^{t+1|t+1} = \frac{2\boldsymbol{I}_{3\times 3} + \delta\boldsymbol{\Theta}_t}{2\boldsymbol{I}_{3\times 3} - \delta\boldsymbol{\Theta}_t} \cdot \boldsymbol{M}_{\text{NED}}^{t+1|t} \quad (51)$$

where

$$\delta\boldsymbol{\Theta}^t = -\begin{bmatrix} 0 & -\delta\boldsymbol{\varphi}^t(2) & \delta\boldsymbol{\varphi}^t(1) \\ \delta\boldsymbol{\varphi}^t(2) & 0 & -\delta\boldsymbol{\varphi}^t(0) \\ -\delta\boldsymbol{\varphi}^t(1) & \delta\boldsymbol{\varphi}^t(0) & 0 \end{bmatrix} \quad (52)$$

where $\delta\boldsymbol{\varphi}^t$, the EKF's error state value for the attitude at the previous time t, is obtained as in (40).

The summary of the real-time dynamic speed of human foot motion localization algorithm, INS/EKF+ZVU+HDR, is presented in Algorithm 2.

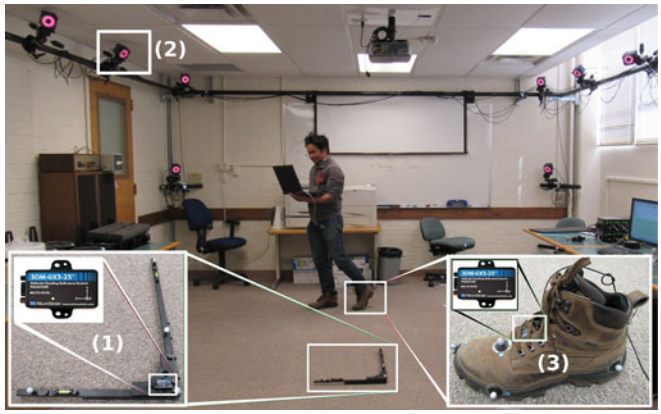

Fig. 7. Using MTS to validate the proposed algorithm.

V. Algorithm Validation With the Ground Truth System

The MTS from Motion Analysis Corporation [40] has a high level of precision, with only a submillimeter error. Therefore, it can be used as ground truth system or an independent and accurate localization system to validate the proposed algorithm. In this validation, the difference between the MTS's results and the proposed algorithm's results on the same coordinate system denotes the error of the proposed algorithm.

For this validation, we setup the experiment as shown in Fig. 7. The configuration of this MTS includes 16 passive optical cameras, which are mounted on the pipe system around the wall of Advanced Robotics and Automation (ARA) lab, as shown in (2) in Fig. 7. Because the shoe needs to be tracked as a rigid body, seven markers are attached to it, as shown in (3) in Fig. 7.

Fig. 8 illustrates the tracking of the movement of the shoe as a rigid body by the MTS.

A. Calibrating the Motion-Tracking System and the Proposed Algorithm

The MTS and the proposed algorithm collect and present data in different coordinate systems. Therefore, for the algorithm's

Algorithm 2: REAL-TIME DYNAMIC SPEED OF HUMAN FOOT MOTION LOCALIZATION ALGORITHM (INS/EKF+ZVU+HDR).

$\boldsymbol{Initiate}$: at time $t+1=1$
$\boldsymbol{v}^{1|0} \leftarrow \mathbf{0}$
$\boldsymbol{p}^{1|0} \leftarrow \mathbf{0}$
$\boldsymbol{M}_{NED}^{1|1} \leftarrow \boldsymbol{M}_{NED}^{1|0}$
$ContinuedLocalization \leftarrow True$
Input: Real-time acceleration, angular rate vectors at time $t+1$ in the IMU body system $\langle a_b^{t+1}, w_b^{t+1}\rangle$
Output: Publish the Real-time velocity, position and attitude in the NED system: $v^{t+1}, p^{t+1}, M_{NED}^{t+1}$
while $ContinuedLocalization = True$ **do**
  $\delta \boldsymbol{X}^{t|t} \leftarrow \delta \boldsymbol{X}^{t}(\delta\boldsymbol{\varphi}^t, \delta\boldsymbol{w}^t, \delta\boldsymbol{p}^t, \delta\boldsymbol{v}^t, \delta\boldsymbol{a}_b^t)$
  //DGP is DynamicStanceDetection() function as presented in Algorithm 1.
  if $DGP(a_b^{t+1}, w_b^{t+1}) = True$ **then**
    $\delta\boldsymbol{v}_b^{t+1|t} \leftarrow \boldsymbol{v}_b^{t+1}$
    $\delta\boldsymbol{w}_b^{t+1|t} \leftarrow \boldsymbol{w}_b^{t+1}$
    $\delta\psi^{t+1} \leftarrow HDR(\delta\psi_{\gamma^{T_i}})$
    $\boldsymbol{m}^{t+1} \leftarrow (\delta\psi^{t+1}, \delta\boldsymbol{w}_b^{t+1|t}, \delta\boldsymbol{v}^{t+1|t})$
  else
    $\boldsymbol{m}^{t+1} \leftarrow \boldsymbol{m}^t$
  $\delta\boldsymbol{X}^{t+1|t} \leftarrow \boldsymbol{\Phi}^{t+1}\delta\boldsymbol{X}^{t|t} + \boldsymbol{n}_t$
  $\boldsymbol{P}^{t|t} \leftarrow (\boldsymbol{I}_{15\times15} - \boldsymbol{K}^t\boldsymbol{H})\boldsymbol{P}^{t|t-1}(\boldsymbol{I}_{15\times15} - \boldsymbol{K}^t\boldsymbol{H})^T + \boldsymbol{K}^t\boldsymbol{R}^t(\boldsymbol{K}^t)^T$
  $\boldsymbol{P}^{t+1|t} \leftarrow \Phi^t\boldsymbol{P}^{t|t}(\Phi^t)^T + \boldsymbol{Q}^t$
  $\boldsymbol{K}^{t+1} \leftarrow \boldsymbol{P}^{t+1|t}\boldsymbol{H}^T(\boldsymbol{H}\boldsymbol{P}^{t+1|t}\boldsymbol{H}^T + \boldsymbol{R}^{t+1})^{-1}$
  $\delta\boldsymbol{X}^{t+1|t+1} \leftarrow \delta\boldsymbol{X}^{t+1|t} + \boldsymbol{K}^{t+1}\cdot[\boldsymbol{m}^{t+1} - \boldsymbol{H}\delta\boldsymbol{X}^{t+1|t}]$
  $\delta\boldsymbol{w}_b^{t+1|t+1} \leftarrow \delta\boldsymbol{X}^{t+1|t+1}(4:6)$
  $\delta\boldsymbol{a}_b^{t+1|t+1} \leftarrow \delta\boldsymbol{X}^{t+1|t+1}(13:15)$
  $\delta\boldsymbol{v}_b^{t+1|t+1} \leftarrow \delta\boldsymbol{X}^{t+1|t+1}(10:12)$
  $\delta\boldsymbol{p}_b^{t+1|t+1} \leftarrow \delta\boldsymbol{X}^{t+1|t+1}(7:9)$
  $\boldsymbol{w}_{b'}^{t+1} \leftarrow \boldsymbol{w}_b^{t+1} - \delta\boldsymbol{w}_b^{t+1|t+1}$
  $\boldsymbol{a}_{b'}^{t+1} \leftarrow \boldsymbol{a}_b^{t+1} - \delta\boldsymbol{a}_b^{t+1|t+1}$
  $\boldsymbol{M}_{NED}^{t+1|t} \leftarrow \boldsymbol{M}_{NED}^{t|t} \cdot \frac{2\boldsymbol{I}_{3\times3}+\delta\boldsymbol{\Omega}_t\cdot\Delta t}{2\boldsymbol{I}_{3\times3}-\delta\boldsymbol{\Omega}_t\cdot\Delta t}$
  $\boldsymbol{a}_e^{t+1} \leftarrow \boldsymbol{M}_{NED}^{t+1|t}\cdot\boldsymbol{a}_{b'}^{t+1} - \boldsymbol{g}_e$
  $\boldsymbol{v}^{t+1|t} \leftarrow \boldsymbol{v}^{t|t} + \boldsymbol{a}_e^{t+1}\cdot\Delta t$
  $\boldsymbol{p}^{t+1|t} \leftarrow \boldsymbol{p}^{t|t} + \boldsymbol{v}^{t+1|t}\cdot\Delta t$
  $\boldsymbol{v}^{t+1|t+1} \leftarrow \boldsymbol{v}^{t+1|t} - \delta\boldsymbol{v}^{t+1|t+1}$
  $\boldsymbol{p}^{t+1|t+1} \leftarrow \boldsymbol{p}^{t+1|t} - \delta\boldsymbol{p}^{t+1|t+1}$
  $\boldsymbol{M}_{NED}^{t+1|t+1} \leftarrow \frac{2\boldsymbol{I}_{3\times3}+\delta\boldsymbol{\Theta}_t}{2\boldsymbol{I}_{3\times3}-\delta\boldsymbol{\Theta}_t}\cdot\boldsymbol{M}_{NED}^{t+1|t}$
  if $QuitLocalization = True$ **then**
    $ContinuedLocalization \leftarrow false$
    $Publish(\boldsymbol{v}^{t+1|t+1}, \boldsymbol{p}^{t+1|t+1}, \boldsymbol{M}_{NED}^{t+1|t+1})$
  else
    $Publish(\boldsymbol{v}^{t+1|t+1}, \boldsymbol{p}^{t+1|t+1}, \boldsymbol{M}_{NED}^{t+1|t+1})$
return *True*

validation, it is important to calibrate them in the same coordinate system. The easiest way to do this is to transform the data of both MTS and the algorithm into the NED system. To transform MTS's data into the NED system, we mounted a 3DM-GX3-25 IMU on an L calibration frame (see (1) in Fig. 7), a tool for calibrating and building the coordinate system of the MTS. This makes the coordinate system of IMU and the L frame equivalent. Therefore, the Euler angles {roll (α), pitch (β), and yaw (γ)} of both the IMU and the MTS are also equivalent. Hence, the rotation matrix $\boldsymbol{R}_M^{t+1}$, which converts the MTS's data from the MTS body system into the MTS's NED system, is obtained by the same formula as $\boldsymbol{M}_{\text{NED}}^{1|0}$ in (39)

$$\boldsymbol{R}_M^{t+1} = \boldsymbol{M}_{\text{NED}}^{1|0}. \tag{53}$$

We name the position collected from the MTS for a marker m at time $t+1$ on the shoe in the MTS's body frame as $\boldsymbol{p}_m^{t+1} = (x_m^{t+1}, y_m^{t+1}, z_m^{t+1})$. The transformed position $\boldsymbol{p}_{m\,\text{NED}}^{t+1}$ of this marker in the MTS's NED system is obtained as

$$\boldsymbol{p}_{m\,\text{NED}}^{t+1} = \boldsymbol{R}_M^{t+1}\boldsymbol{p}_m^{t+1}. \tag{54}$$

The IMU's moving point $\boldsymbol{p}^{t+1|t+1}$ in the proposed algorithm at time $t+1$ is obtained as in (50). Because the markers and IMU are mounted on the same shoe, the starting points of the marker m and IMU in the proposed algorithm at starting time $t+1=0$ are equivalent, $\boldsymbol{p}_{m\,\text{NED}}^{0} = \boldsymbol{p}^{0|0}$. Otherwise, $\boldsymbol{p}^{0|0}$ is the original point in the IMU's NED system. Hence, it is necessary to transform the original position of the IMU's NED system into the MTS's NED system as follows:

$$\boldsymbol{p}_{m\,\text{NED.IMU}}^{t+1} = \boldsymbol{p}^{t+1|t+1} + \boldsymbol{p}_{m\,\text{NED}}^{0}. \tag{55}$$

After transforming the data of both the MTS and the IMU algorithm into the same coordinate system by (54) and (55), we plot them on the same figure (see Fig. 9) to compare their accuracy.

In Fig. 9, the dashed-dotted line and solid line present the trajectories tracked by the MTS and the proposed IMU algorithm,

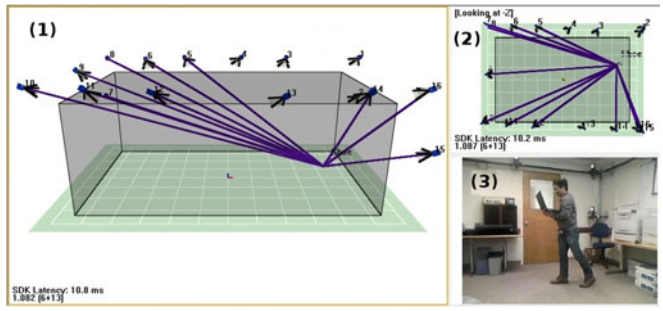

Fig. 8. Tracking of shoe's movement around the ARA lab by MTS.

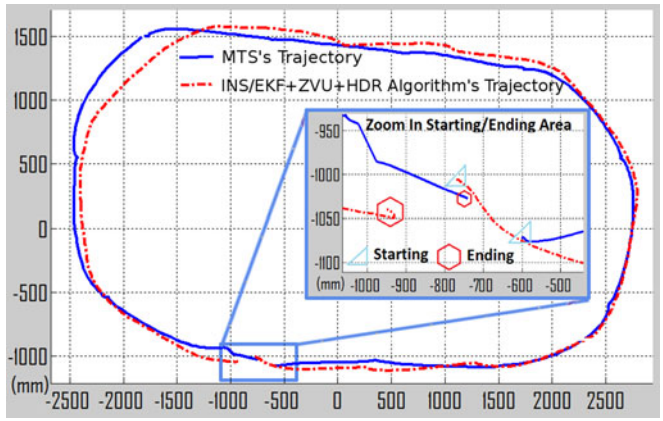

Fig. 9. Plotting the trajectories of both MTS and the proposed algorithm.

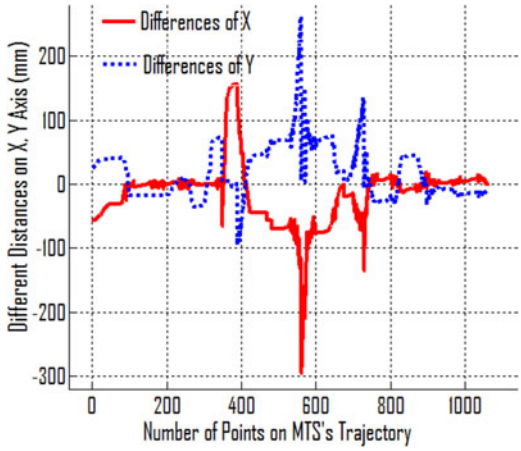

Fig. 10. Error between MTS and the proposed algorithm trajectories along x- and y-axes.

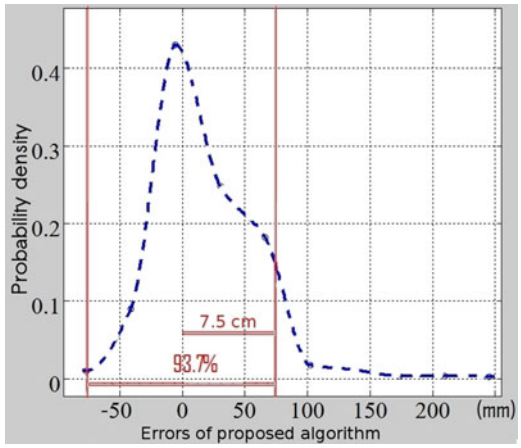

Fig. 11. Convergence of the proposed algorithm is over 93% for an error range of 7.5 cm around MTS's results.

respectively. The exact difference between these trajectories denotes the error of the proposed algorithm. In this validation, the difference distance is 45 mm, whereas the traveling distance around the ARA lab is 13.4 m. Therefore, the average error in the total traveling distance is approximately 0.335%. To further demonstrate the validity of the proposed algorithm, we plotted the trajectory error between the MTS and the proposed algorithm along x- and y-axes (see Fig. 10) and found that the maximum error is small, around 280 mm.

B. Empirical Demonstration of Convergence

To demonstrate the convergence of the proposed algorithm in the MTS, we use the probability density of the difference between them. The difference function is obtained as follows:

$$\boldsymbol{diff}(\boldsymbol{p}_{m\,\mathrm{NED}}^{t+1}, \boldsymbol{p}_{m\,\mathrm{NED.IMU}}^{t+1}) = (\boldsymbol{p}_{m\,\mathrm{NED}}^{t+1} - \boldsymbol{p}_{m\,\mathrm{NED.IMU}}^{t+1}). \quad (56)$$

The probability density of the differences is computed by

$$\boldsymbol{prob}_{\mathrm{MTS.IMU}} = \frac{\boldsymbol{f}(\boldsymbol{diff}(\boldsymbol{p}_{m\,\mathrm{NED}}^{t+1}, \boldsymbol{p}_{m\,\mathrm{NED.IMU}}^{t+1}))}{n} \quad (57)$$

where $\boldsymbol{f}$ is the frequency function, and n is the number of points on the MTS's trajectory, $\{\boldsymbol{p}_{m\,\mathrm{NED}}^{t+1}\}$, and $t+1 \in \{1, 2, ..., n\}$. Because the responding rates of the MTS and the IMU are different, and the MTS is considered as the ground truth for this validation, the number of total elements n in (57) is exactly the same as the number of total elements in the MTS's dataset $\{\boldsymbol{p}_{m\,\mathrm{NED}}^{t+1}\}$. The results of the probability density, plotted in Fig. 11, prove the convergence of the proposed algorithm with the MTS's results (93.7% of the proposed algorithm's results are convergent with MTS's results in the small error range of less than 7.5 cm).

VI. Experimental Results

In this section, we implement the proposed algorithm (INS/EKF+ZVU+HDR) and compare it with two other algorithms: the INS/ZVU and the INS/ZVU+HDR. For this, we mount a MicroStrain 3DM-GX3-25 IMU sensor on the shoe for testing them (see (3) in Fig. 7). The specifications of this IMU

TABLE I
MicroStrain 3DM-GX3-25 IMU's General Information

Specifications	Values
Data output rate	up to 1000 Hz
Baud rate	115 200 to 921 600 bps
Power consumption	80 mA @ 5 V with USB

TABLE II
MicroStrain 3DM-GX3-25 IMU's Specifications

Specifications	Accels	Gyros	Mags
Measure range	±5 g	±300°/s	±2.5G
Nonlinearity	±0.1% fs	±0.03% fs	±0.4% fs
Bias stability	±0.04 mg	18 °/h	
Initial bias	±0.002 g	±0.25 °/s	±0.003 G
Factor stability	±0.05%	±0.05%	±0.1%
Noise density	80 μg/$\sqrt{\text{Hz}}$	0.03 °/s/$\sqrt{\text{Hz}}$	100 μG/$\sqrt{\text{Hz}}$
Alignment error	±0.05°	±0.05°	±0.05°
Sampling rate	30 kHz	30 kHz	7.5 kHz

are presented in Tables I and II. We implement the algorithms in the C++ language and run them on the Hydro Robotic Operating System platform. The real-time stream data from this 3DM-GX3-25 IMU sensor is processed by the proposed algorithm. We initialized the process noise covariance matrix $\boldsymbol{Q}^0 = \mathrm{diag}(10^{-4}, 10^{-4}, 10^{-4}, 0, 0, 0, 0, 0, 0, 10^{-4}, 10^{-4}, 10^{-4}, 0, 0, 0)$. The measurement noise covariance matrix $\boldsymbol{R}^0$ and the estimated error covariance matrix $\boldsymbol{P}^{0|0}$ are initialized by (42) and (43), respectively.

A. Indoor Localization Tests

We tested the algorithms with different walking speeds in the hallway on the third floor of the Scrugham Engineering and Mines (SEM) building at the UNR campus.

Fig. 12 shows the results of comparison among the three algorithms: INS/ZVU, INS/ZVU+HDR, and INS/EKF+ZVU+HDR. It can be seen that the INS/EKF+ZVU

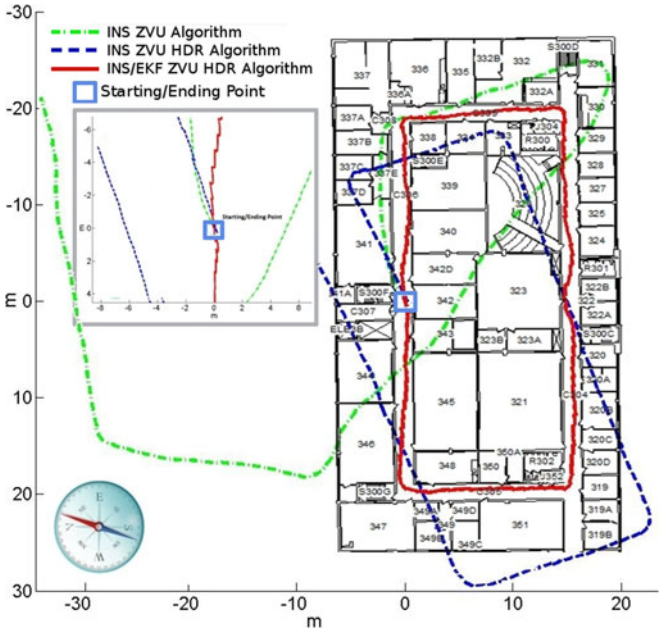

Fig. 12. Two-dimensional trajectories plotted on the hallway of the third floor, SEM building, UNR campus.

+HDR algorithm outperforms the other two, because its walking trajectory closely matches with the hallway of the SEM building. The average difference in distance between the starting and the ending points in the 2-D coordinate system for real-time dynamic INS/EKF ZVU HDR algorithm is about 0.45 m over 120 m, which is equivalent to 0.375% error.

To further demonstrate the effectiveness of the proposed INS/EKF+ZVU+HDR algorithm, we tested it with different walking speeds: slow (0.58 m/s), normal (1.28 m/s), and fast (1.79 m/s). The results are plotted in Fig. 13. The normal speed trajectory (the green line) shows up as a slightly better fit than the other speed trajectories in the hallway. The errors for normal and fast speeds, ranging from 0.45 m to 0.51 m over 120 m, equivalent to around 0.375% error, are still considered good.

B. Outdoor Localization Tests

For outdoor environments, we tested and compared the proposed algorithm with the others over a larger scale trajectory along the sidewalks of the UNR campus. The results are plotted in Fig. 14. The average difference in distance between the starting and the ending points in the 2-D coordinate system for real-time dynamic INS/EKF+ZVU+HDR is about 3.59 m over 645 m, equivalent to 0.55% error. The zoom-in area "A" (see Fig. 14) is the starting/ending point of the testing path on the UNR campus, whereas point "B" is the area, which shows walking through the building gate of a UNR building. Large noise of local magnetic disturbances can be seen around point "B" (see Fig. 15) because of large steel frames used in the nearby construction. This caused the trajectories of the INS/ZVU and INS/ZVU+HDR algorithms to completely turn in the wrong directions, whereas the trajectory of the INS/EKF+ZVU+HDR algorithm remained excellent.

Fig. 13. Two-dimensional trajectories of different speeds.

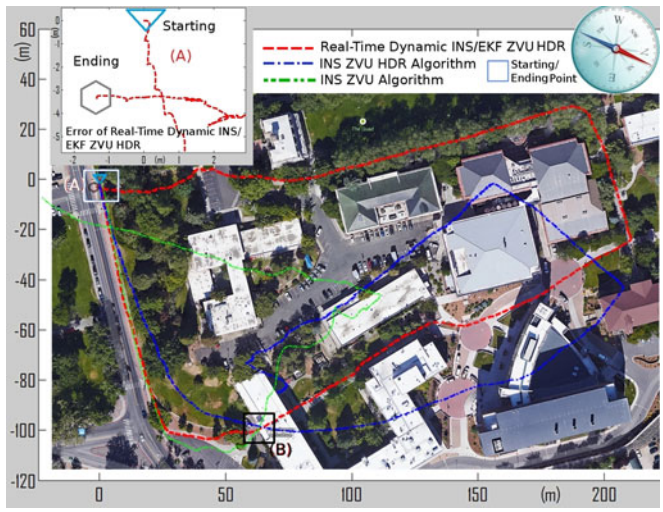

Fig. 14. Two-dimensional trajectories of outdoor testing along the sidewalks on the UNR campus.

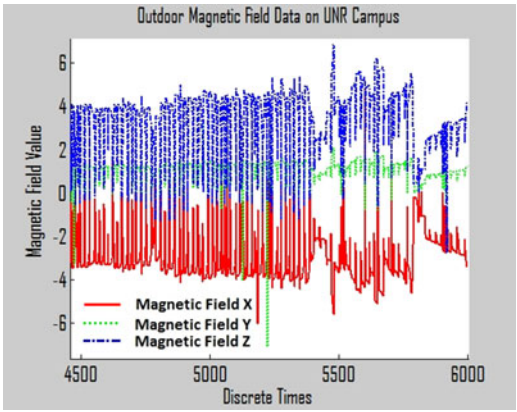

Fig. 15. Outdoor magnetic field data around point (B) in Fig. 14.

VII. Conclusion and Future Work

In this paper, we have proposed a real-time human foot motion localization algorithm, which integrates the dynamic GPD, the ZVU, the HDR, and the EKF. As a result of this integration, the proposed algorithm could remove most of the IMU's heading drifts, as well as the magnetic noise of both indoor and outdoor environments. The proposed algorithm could accurately estimate, in real time, the human foot position, velocity, and attitude in dynamic motion speeds. Moreover, it has been validated by an independent and accurate localization system. To demonstrate the effectiveness of the proposed algorithm, real-time localization tests have been conducted in both indoor and outdoor environments with the existing of magnetic disturbances.

Motivated by recent advances in the development of embedded technology in human–machine systems, inertial/IMU sensors are embedded in smart and wearable devices, such as shoes, watches, phones, band aids, etc., to support human daily activity. We expect that the proposed human foot gait detection and localization algorithm will further contribute to support human life in general, and elderly people in particular, who may need wearable technologies to make their life easier.

Human localization in both indoor and outdoor/GPS-outage environments has always been an important and challenging problem. Our proposed human foot localization algorithm provides a solution to this problem, and we expect that this algorithm will open up new vista for more effective indoor/outdoor human tracking in matters relating to medicine, healthcare, business logistics, and possibly entertainment.

Although the proposed algorithm targets environments with no support from other sensors, such as GPS, radio tracking systems, cameras, etc., it is possible to integrate it with these sensors to enhance the performance of human foot localization over long distances.

References

[1] C. Randell, C. Djiallis, and H. Muller, "Personal position measurement using dead reckoning," in *Proc. 7th IEEE Int. Symp. Wearable Comput.*, 2003, pp. 166–173.

[2] C. Toth, D. A. Grejner-Brzezinska, and S. Moafipoor, "Pedestrian tracking and navigation using neural networks and fuzzy logic," in *Proc. IEEE Int. Symp. Intell. Signal Process.*, 2007, pp. 1–6.

[3] A. R. Jimenez, F. Seco, C. Prieto, and J. Guevara, "A comparison of pedestrian dead-reckoning algorithms using a low-cost MEMS IMU," in *Proc. IEEE Int. Symp. Intell. Signal Process.*, 2009, pp. 37–42.

[4] L. Klingbeil and T. Wark, "A wireless sensor network for real-time indoor localisation and motion monitoring," in *Proc. 7th Int. Conf. Inf. Process. Sens. Netw*, May 2008, pp. 39–50.

[5] J. Corrales, F. Candelas, and F. Torres, "Hybrid tracking of human operators using IMU/UWB data fusion by a Kalman filter," in *Proc. ACM/IEEE Int. Conf. Human Robot Interact.*, 2008, pp. 193–200.

[6] A. Ruiz, F. Granja, J. Honorato, and J. Rosas, "Accurate pedestrian indoor navigation by tightly coupling foot-mounted IMU and RFID measurements," *IEEE Trans. Instrum. Meas.*, vol. 61, no. 1, pp. 178–189, Jan. 2012.

[7] L. Fang *et al.*, "Design of a wireless assisted pedestrian dead reckoning system—The NavMote experience," *IEEE Trans. Instrum. Meas.*, vol. 54, no. 6, pp. 2342–2358, Dec. 2005.

[8] S. Godha, G. Lachapelle, and M. E. Cannon, "Integrated GPS/INS system for pedestrian navigation in a signal degraded environment," in *Proc. Inst. Navigat. GNSS Conf.*, 2006, pp. 26–29.

[9] J. Schmid, M. Volker, T. Gadeke, P. Weber, W. Stork, and K. D. Muller-Glaser, "An approach to infrastructure-independent person localization with an IEEE 802.15.4 WSN," in *Proc. Int. Conf. Indoor Positioning Indoor Navigat.*, Sep. 2010, pp. 1–9.

[10] J. Saarinen, J. Suomela, S. Heikkila, M. Elomaa, and A. Halme, "Personal navigation system," in *Proc. IEEE/RSJ Int. Conf. Intell. Robots Syst.*, 2004, pp. 212–217.

[11] J. Biswas and M. Veloso, "Depth camera based indoor mobile robot localization and navigation," in *Proc. IEEE Int. Conf. Robot. Autom.*, May 2012, pp. 1697–1702.

[12] I. Skog, P. Handel, J. Nilsson, and J. Rantakokko, "Zero-velocity detection—An algorithm evaluation," *IEEE Trans. Biomed. Eng.*, vol. 57, no. 11, pp. 2657–2666, Nov. 2010.

[13] A. R. Jimenez, F. Seco, J. C. Prieto, and J. Guevara, "Indoor pedestrian navigation using an INS/EKF framework for yaw drift reduction and a foot-mounted IMU," *Proc. 7th Workshop IEEE Positioning Navigat. Commun.*, 2010, pp. 135–143.

[14] X. Yun, J. Calusdian, E. R. Bachmann, and R. B. McGhee, "Estimation of human foot motion during normal walking using inertial and magnetic sensor measurements," *IEEE Trans. Instrum. Meas.*, vol. 61, no. 7, pp. 2059–2072, Jul. 2012.

[15] E. Foxlin, "Pedestrian tracking with shoe-mounted inertial sensors," *IEEE Comput. Graph. Appl.*, vol. 25, no. 6, pp. 38–46, Nov./Dec. 2005.

[16] Q. Yuan, I. M. Chen, and S. P. Lee, "SLAC: 3D localization of human based on kinetic human movement capture," in *Proc. IEEE Int. Conf. Robot. Autom.*, May 2011, pp. 848–853.

[17] F. Hoflinger, R. Zhang, and L. M. Reindl, "Indoor-localization system using a micro-inertial measurement unit (IMU)," in *Proc. Eur. Freq. Time Forum*, Apr. 2012, pp. 443–447.

[18] H. Fourati, N. Manamanni, L. Afilal, and Y. Handrich, "Position estimation approach by complementary filter-aided IMU for indoor environment," in *Proc. Eur. Control Conf.*, Jul. 2013, pp. 4208–4213.

[19] S. Soo and S. Park, "Pedestrian inertial navigation with gait phase detection assisted zero velocity updating," in *Proc. 4th Int. Conf. Auton. Robots Agents*, May 2009, pp. 336–341.

[20] C. Randell, C. Djiallis, and H. Muller, "Personal position measurement using dead reckoning," in *Proc. 7th IEEE Int. Symp. Wearable Comput.*, 2003, pp. 166–173.

[21] F. Cavallo, A. Sabatini, and V. Genovese, "A step toward GPS/INS personal navigation systems: Real-time assessment of gait by foot inertial sensing," in *Proc. IEEE/RSJ Int. Conf. Intell. Robots Syst.*, 2005, pp. 1187–1191.

[22] S. Park, "Pedestrian inertial navigation with gait phase detection assisted zero velocity updating," in *Proc. 4th Int. Conf. Auton. Robots Agents*, Feb. 2000, pp. 336–341.

[23] L. Ojeda and J. Borenstein, "Non-GPS navigation with the personal dead-reckoning system," *Proc. SPIE*, vol. 6561, p. 65610C, 2007.

[24] U. Steinhoff and B. Schiele, "Dead reckoning from the pocket—An experimental study," in *Proc. IEEE Int. Conf.*, Apr. 2010, pp. 162–170.

[25] A. T. Erdem and A.O. Ercan, "Fusing inertial sensor data in an extended Kalman filter for 3D camera tracking," *IEEE Trans. Image Process.*, vol. 24, no. 2, pp. 538–548, Feb. 2015.

[26] G. Welch and G. Bishop, "An Introduction to the Kalman Filter," Chapel Hill, NC, USA: Univ. North Carolina, Rep. TR-95-041, 1995, pp. 1–16.

[27] S. Bolognani, L. Tubiana, and M. Zigliotto, "Extended Kalman filter tuning in sensorless PMSM drives," *IEEE Trans. Ind. Appl.*, vol. 39, no. 6, pp. 1741–1747, Nov./Dec. 2003.
[28] F. Zampella, M. Khider, P. Robertson, and A. Jimenez, "Unscented Kalman filter and magnetic angular rate update (MARU) for an improved pedestrian dead-reckoning," in *Proc. IEEE/ION Position Location Navigat. Symp.*, Apr. 2012, pp. 129–139.
[29] S. Beauregard and M. Widyawan, "Indoor PDR performance enhancement using minimal map information and particle filters," in *Proc. IEEE/ION Position Location Navigat. Symp.*, May 2008, pp. 141–147.
[30] L. Nguyen and H. M. La, "Development of a smart shoe for building a real-time 3D map," in *Proc. 32st Int. Symp. Autom. Robot. Construction Mining*, Jun. 2015, pp. 1–8.
[31] L. V. Nguyen, H. M. La, J. Sanchez, and T. Vu, (2016, Apr.). A smart shoe for building a real-time 3D map, *Autom. Construction*, [Online]. pp. 1–11. Available: http://www.sciencedirect.com/science/article/pii/S0926580516300401
[32] J. Juen, Q. Cheng, V. Prieto-Centurion, J. A. Krishnan, and B. Schatz, "Health monitors for chronic disease by gait analysis with mobile phones," *Telemed. J. e-Health*, vol. 20, pp. 1035–1041, Nov. 2014.
[33] J. P. Azulay *et al.*, "Automatic motion analysis of gait in patients with parkinson disease: Effects of Levodopa and visual stimulations," *Rev. Neurol.*, vol. 152, pp. 128–134, Feb. 1996.
[34] Q. Yuan and I-M. Chen, "3-D localization of human based on an inertial capture system," *IEEE Trans. Robot.*, vol. 29, no. 3, pp. 806–812, Jun. 2013.
[35] M. Swangnetr and D. B. Kaber, "Emotional state classification in patient–robot interaction using wavelet analysis and statistics-based feature selection," *IEEE Trans. Human-Mach. Syst.*, vol. 43, no. 1, pp. 63–75, Jan. 2013.
[36] L. Nguyen, H. M. La, and T. H. Duong, "Dynamic human gait phase detection algorithm," in *Proc. ISSAT Int. Conf. Model. Complex Syst. Environ.*, Jun. 2015, pp. 1–5.
[37] H. Zhang, J. Qian, L. Shen, and Y. Zhang, "Research on healthy subject gait cycle phase at different walking speeds," in *Proc. IEEE Int. Conf. Robot. Biomimetics*, Dec. 2012, pp. 1349–1354.
[38] W. George and II, Collins, *The Foundations of Celestial Mechanics*. Tucson, AZ, USA: Pachart, 2004.
[39] J. Borestein, L. Ojeda, and S. Kwanmuang, "Heuristic reduction of gyro drift in IMU-based personnel tracking system," *Proc. SPIE*, vol. 7306, p. 73061H, May 2009.
[40] Motion Tracking System—Motion Analysis Corporation. (2016). [Online]. Available: http://www.motionanalysis.com

Luan Van Nguyen received the B.S. and M.S. degrees in computer science from Vietnam National University, Hanoi, Vietnam, in 1999 and 2006, respectively, and the M.S. degree in computer science from Rutgers University, New Brunswick, NJ, USA, in 2014. He is currently working toward the Ph.D. degree in the Advanced Robotics and Automation Laboratory, Department of Computer Science and Engineering, University of Nevada, Reno, NV, USA.

His research interests include human–machine systems, robotics, and human–robot interaction.

Hung Manh La (M'09–SM'14) received the B.S. and M.S. degrees in electrical engineering from the Thai Nguyen University of Technology, Thai Nguyen, Vietnam, in 2001 and 2003, respectively, and the Ph.D. degree in electrical and computer engineering from Oklahoma State University, Stillwater, OK, USA, in 2011.

He is the Director of the Advanced Robotics and Automation Laboratory and an Assistant Professor in the Department of Computer Science and Engineering, University of Nevada, Reno, NV, USA. From 2011 to 2014, he was a Postdoctoral Research Fellow and then a Research Faculty Member with the Center for Advanced Infrastructure and Transportation, Rutgers University, Piscataway NJ, USA. He has authored more than 50 papers published in major journals, as book chapters, and in international conference proceedings. His current research interests include robotic systems and mobile sensor networks.

Dr. La received the 2014 ASCE Charles Pankow Award for the Robotics Assisted Bridge Inspection Tool, three Best Paper Awards, and Best Presentation Awards at international conferences. He is an Associate Editor of the IEEE TRANSACTIONS ON HUMAN-MACHINE SYSTEMS and a Guest Editor of the *International Journal of Robust and Nonlinear Control*.